



Motion of a sphere in a viscous fluid towards a wall confined versus unconfined conditions

I. Fonceca¹ · R. C. Hidalgo¹ · D. Maza¹

Received: 12 July 2021 / Accepted: 20 December 2021 / Published online: 6 February 2022
© The Author(s) 2022

Abstract

In the present work, we investigate experimentally and numerically the motion of solid macroscopic spheres (Brownian and colloidal effects are negligible) when settling from rest in a quiescent fluid toward a solid wall under confined and unconfined configurations. Particle trajectories for spheres of two types of materials are measured using a high-speed digital camera. For unconfined configurations, our experimental findings are in excellent agreement with well-established analytical frameworks, used to describe the forces acting on the sphere. Besides, the experimental values of the terminal velocity obtained for different confinements are also in very good agreement with previous theoretical formulations. Similar conditions are simulated using a resolved CFD-DEM approach. After adjusting the parameters of the numerical model, we analyze the particle dynamic under several confinement conditions. The simulations results are contrasted with the experimental findings, obtaining a good agreement. We analyze several systems varying the radius of the bead and show the excellent agreement of our results with previous analytical approaches. However, the results indicate that confined particles have a distinct dynamics response when approaching the wall. Consequently, their motion cannot be described by the analytical framework introduced for the infinite system. Indeed, the confinement strongly affects the spatial scale where the particle is affected by the bottom wall and, accordingly, the dimensionless results can not be collapsed in a single master curve, using the particle size as a characteristic length. Alternatively, we rationalize our findings using a kinematic approximation to highlight the relevant scale of the problem. Our outcomes suggest it is possible to determine a new spatial scale to describe the collisional process, depending on the specific confining conditions.

Keywords Sphere towards a plane · Newtonian fluids · Lubrication · Stokes flows

1 Introduction

Stokes' law establishes the fluid resistance acting on a sphere when moving through a viscous liquid with a low Reynolds number. Its derivation assumes a fixed, rigid sphere immersed in a uniform velocity field with infinite dimensions [1]. However, in most practical cases, there is movement of both particle and fluid, and the system is bounded by walls [2]. These factors inevitably affect the motion of the sphere, inducing a wall-bounded flow around the particles and requiring corrections to the drag formula. In any case, the underlying principles of Stokes' law have notably helped

developing more elaborated approaches used in industrial applications [3].

In another limit, the rheological behavior of dense suspensions under confinement is often intriguing. For instance, common sense suggests that inertial effects should have no relevance for minimal shear rates. However, several studies with microfluidic systems have demonstrated that a small inertial contribution can give rise to a variety of exciting effects. For instance, shear-induced migration, particle segregation, and shear thickening have been experimentally observed [4–8]. In fact, characterizing the single-particle dynamics in confined conditions is paramount to defining a baseline for understanding dense scenarios in which many particles interact between them and also with the system boundaries. Typically, the results for the particle trajectories are acquired with acoustic methods, magnetic interferometry, or direct optical measurements [9–14].

✉ I. Fonceca
jfonceca@alumni.unav.es

¹ Department of Physics and Applied Mathematics, University of Navarra, Pamplona, Spain

In addition, particle–particle and particle–wall collisions play an essential role in many processes involving particle suspensions. At very low Reynolds conditions, the movement of a single sphere settling towards a wall is an old but still exciting topic [15–18]. These theoretical frameworks accurately resolve the flow field around the particle, helping to predict the hydrodynamic coupling between the particle and the fluid. There are many results in the literature for the influence of the confinement on the dynamics of particles. For instance, the motion of spheres under confined configurations has been analyzed for parallel planar walls [19, 20], cylindrical containers [10, 21], and rough walls [22]. However, a significantly lower number of studies have explored the settling of particles toward a wall under confined conditions. It is worth mentioning the efforts of studying spheres settling in pipes [10, 23], spheres in conical containers [24], sphero-cylindrical particles in cylindrical containers [25]. Moreover, Despeyroux et al. investigated the settling of spheres confined in a cylindrical container using a non-newtonian fluid [26].

It is known that adding suspended particles to a fluid typically increases its viscosity. On top of this, the intrinsic lack of scale of particulate systems is very relevant when these systems are forced to pass through constrictions where particle clogging events can occur. So far, the majority of the studies have mainly centered on the consequences of the blockage process on the global flowing properties [27, 28]. However, Agbangla et.al. [29] numerically analyzed the collective hydrodynamic effects of microparticles moving through a pore. They found very stable clogged structures induced by strong particle-particle interaction and particle-wall adhesion, which prevents rearrangements of particles within an aggregate and enhances the clog’s stability. Moreover, van de Laar et al. [30] performed microfluidic real-time imaging to capture the influence of pore geometry and particle interactions on suspension clogging in constrictions. In general, it is accepted that the clogging (or jamming) process is mainly governed by the driven force acting on the particles, the long-range hydrodynamic interactions, and the nature of the particle-particle and particle-wall interactions [29–33]. Here, we examine experimentally and numerically the impact of the lateral confinement on the particle deceleration process when it settles from rest in a quiescent fluid toward a solid flat wall.

The manuscript is organized as follows: in Sect. 1.1 we discuss the set of analytical models used to describe the settling of spheres for different geometries. Next, we discuss the relevant details of our experimental setup (Sect. 2) and numerical model (Sect. 3). Then, we present the results and discussions in Sect. 4, contrasting the experimental and numerical data. Lastly, we summarize our findings and present the future perspectives of the present work.

1.1 Dynamics of the particle settling through a viscous fluid

The present research effort is focused on the collision of a sphere that moves in a quiescent fluid, approaching a bottom wall in confined and unconfined conditions. Figure 1 depicts a sphere settling at a distance h_z from the bottom wall, and confined on the x - and y -axis directions by parallel plates separated by a distance W . Figure 1a is a 2D view and Fig. 1b is a 3D view. Note, that unconfined conditions corresponds to $(\frac{W}{2R} \gg 1)$.

In general, Newton’s law describing the translational motion of the sphere reads as follows:

$$(jm_f + m_p) \frac{dv}{dt} = F_d + F_b + mg \tag{1}$$

where the added mass correction jm_f has been introduced to take into account the inertial force of the fluid mass around the particle [34]. Typically, the dimensionless coefficient $j = 0.5$ for dense spheres. Besides this, m_f is the added mass, g accounts for the gravity field, F_b is the buoyant force and F_d is the drag force. It is known that the magnitude of F_d is dependent on the liquid viscosity μ , the particle radius R , and the distances from the lateral and bottom walls.

For a long time ago, it has been understood that confinement increases viscous friction, reducing the settling velocity compared to unconfined cases. In 1923, Faxén introduced a theoretical framework for a sphere moving along the center-line between parallel walls, but far from the bottom wall ($h_z \rightarrow \infty$), resulting in the following drag force:

$$F_d = -6\pi\mu Rvf(s)$$

$$f(s) = \frac{1}{1 - 1.004s + 0.1475s^2 - 0.131s^4 - 0.0644s^5} \tag{2}$$

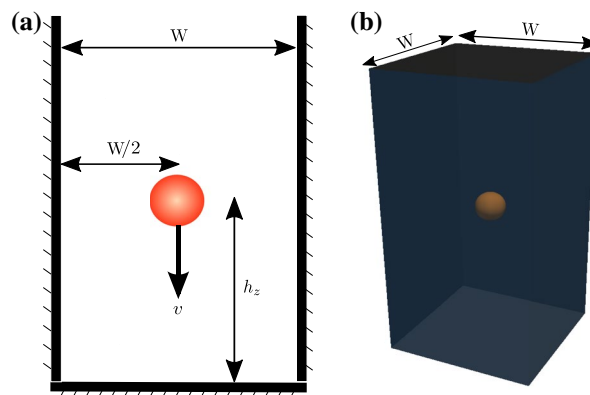


Fig. 1 A sphere sedimenting towards the bottom wall at the center-line between parallel walls a 2D and b 3D representation

where $s = \frac{d}{W}$ accounts for the magnitude of the confinement [2], and possibly allowing the introduction of an effective viscosity $\mu_{eff} = \mu f(s)$. Faxén’s solution was later found to be applicable only when $W \gg d$, while Ganatos et. al. introduced a generalized solution, which is suitable for closer particle-to-wall spacing [35].

After these seminal works, a notably large number of works have been devoted to developing their ideas, although many open questions about the mechanisms of energy dissipation remain unsolved. Consider, for instance, a settling sphere centered in a tall cylindrical pipe of diameter D . Under this condition Haberman and Sayre [21] provided a correction factor K_p for the drag force in the limit of low Reynolds numbers:

$$F_d = -3\pi\mu d v K_p$$

$$K_p = \frac{1 - 0.75875(d/D)^5}{1 - 2.1050(d/D) + 2.0865(d/D)^3 - 1.7068(d/D)^5} \tag{3}$$

A thorough list of correction functions for the lateral confinement on the settling velocity was published by Arsenijević et. al. [36].

Another still open problem regarding particle-fluid interactions concerns the influence of surrounding fluid on the collision dynamics of the immersed particles. Early last century, Lorentz described analytically the motion of a particle sedimenting in a laterally unbounded fluid and settling towards a wall [15], and long afterwards, in 1961, Brenner introduced a better approach for the same system but requiring no assumptions concerning the distance to the boundaries [16]. The obtained expression for the drag force reads as:

$$F_d = -6\pi\mu R v \lambda(h_z) \tag{4}$$

where λ is:

$$\lambda = \frac{4}{3} \sinh(\alpha) \sum_{n=1}^{\infty} \frac{n(n+1)}{(2n-1)(2n+3)} \left[\frac{2 \sinh[(2n+1)\alpha] + (2n+1) \sinh(2\alpha)}{4 \sinh^2[(n+0.5)\alpha] - (2n+1)^2 \sinh^2(\alpha)} - 1 \right], \tag{5}$$

and $\alpha = \cosh^{-1}(h_z/R)$ is the angular component in bipolar coordinates. Note that in the case $\lim_{h_z \rightarrow \infty} \lambda(h_z) = 1$, Eq. (4) reduces to the well-known Stokes’ law [1]. Hence, the parameter λ is interpreted as the correction factor to the Stokes’ drag force, considering the gap $z = h_z - R$ between the particle and the bottom wall.

This procedure indicates that as the sphere approaches the wall, it experiences a diverging drag force, which prevents the surfaces from making contact with each other [37]. Exploring the high Reynolds limit response, a series of experimental and numerical efforts have been done [11,

37–39]. In this other limit, particles collide with the wall with non-zero velocity, indicating that a finite force acts on the sphere at all times. An exhaustive discussion of the formal theoretical aspects regarding the particle fluid interaction hydrodynamics and the available approximations to deal with it can be found in Kim & Karrila’s book [40].

It is worth mentioning that the details of the particle-wall collision under confinement are less theoretically explored [20, 41]. Brenner suggested that the combined action of lateral walls and the bottom wall can be considered as a linear superposition of both effects [16], but to our best knowledge, there are no existing systematic studies devoted to this limit. Accordingly, we examine the dynamics of a particle settling in liquid towards a rigid wall in this manuscript, varying the confinement levels systematically. We implement an experimental setup to measure the influence of the confinement on the particle bottom wall collisional dynamics and numerically simulate the analogous situation by a hybrid CFD-DEM approach. Importantly, the numerical protocol allows to quantify the dynamics of the fluid, assessing the stress distribution around the particle, which determines the energy dissipation mechanisms.

2 Experimental setup

The experiment consists of recording a solid sphere sedimenting motion in a fluid onto a solid wall. We use steel spherical beads of radius $R = \{0.5, 1.0, 1.5\}$ mm with density $\rho_p = 7.605 \pm 0.005$ g/cm³, sedimenting in a silicon oil with kinematic viscosity $\nu = 1000$ cSt (Sigma-Aldrich™). We also use plastic spheres with radius $R = 1.0$ mm and density $\rho_p = 2.210 \pm 0.005$ g/cm³. We assume that surface forces such as Van der Waals, attractive, or electrical double layer repulsive forces are negligible for the radius used in our experiments.

Figure 2 shows one of the containers used during the experiments. In our analysis, the container width W varies systematically, thus allowing the assessment of different confinement conditions. In all cases, the container is filled to the same liquid height. Specifically, we use three different cells: $10 \times 10 \times 10$ cm and $2 \times 2 \times 5$ cm acrylic boxes and a $1 \times 1 \times 5$ cm quartz cuvette (Fig. 2). The optical quality of the used material allows for a direct recording of the particle trajectory. The spheres is released from an adjustable lid with an aperture in its center. For all beads, the aperture diameter is not larger than $d_h = 2.25R$; hence the off-center particle misalignment against the cell axis is less than the bead radius.

A Photron FASTCAM Mini UX100™ high-speed video camera is used to record particle motion with a 1280×1024 pixels image resolution. Images are analyzed with the Photron FASTCAM Analysis™ software, extracting the location of

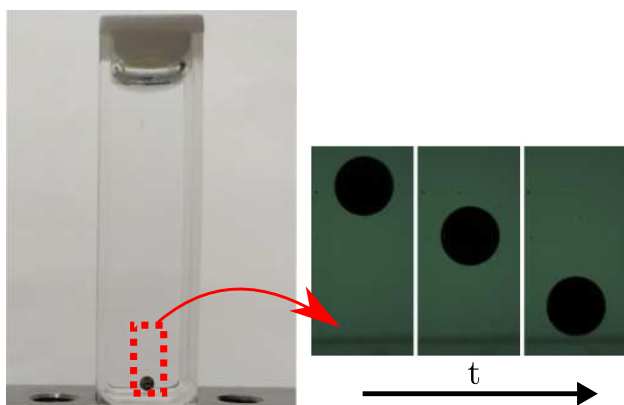


Fig. 2 Experimental setup for the 1 × 1 × 5 cm quartz cuvette

the particle center frame by frame. Depending on the field of view used to track the motion of the bead, the centroid detection procedure imposes spatio-temporal resolution and corresponding errors. Another relevant aspect when accounting for errors is the definition of the reference position ($z = 0$). In the literature, we find an example of the importance of measuring with good precision the reference position [13] to determine correct dynamics of the particle when $z/R \ll 1$. In Table 1 we report for each set of experimental realization the corresponding resolutions, errors and reference position precision. In a typical particle-wall collision sequence, particle velocities $v(t)$ and accelerations $a(t)$ are computed as the temporal derivatives of successive coordinates. After that, results are processed by a simple moving average protocol in order to smooth the results. Despite the dispersion in the magnitudes of the calculated instantaneous particle velocities, the correlation between time and vertical coordinate (h_z) is always linear when the particle falls down a typical distance of ten times its diameter after the initial contact with the free surface (Pearson’s correlation factor is larger than 0.999 for all the studied situations). Accordingly, we will assume the fitted slope of this evolution as particle terminal velocity, v^* . It is worth noting that the short acceleration process until reaching the limit velocity is not assessed ignoring an initial displacement equal to the particle diameter. In all cases, the experiments are repeated three times to guarantee the reproducibility of the results.

3 Numerical method

The numerical algorithm is an extension of the well-established CFDEM@coupling framework [42]. This approach can handle the movement of spherical particles with density ρ_p embedded in a Newtonian fluid with kinematic viscosity ν . The software combines the Computational Fluid Dynamics (CFD) solving capabilities of OpenFOAM [43] with a Discrete Element Method (DEM) implementation in LIGGGHTS [42], which addresses the motion of each particle. Our approach explicitly introduces a body force term when solving the Navier-Stokes Equation, and applies the viscous and strain components of the stresses acting on the particle. This procedure has been more reliable in resolving the stokesian behavior of a particle settling in a quiescent fluid [44–46]. Describing the fluid phase, the incompressible Navier-Stokes equation including the gravitational body force reads as:

$$\rho_f \frac{\partial \mathbf{U}}{\partial t} + \rho_f (\mathbf{U} \cdot \nabla) \mathbf{U} = -\nabla p + \mu \nabla^2 \mathbf{U} + \rho_f \mathbf{g}. \tag{6}$$

Additionally, the continuity equation also holds:

$$\nabla \cdot \mathbf{U} = 0 \tag{7}$$

The particles are inserted at specific locations in the continuous CFD domain. Thus, the solid-particle occupation region \mathcal{T}_i is defined using a void fraction field Φ . At the points occupied by solid particles (nodes inside \mathcal{T}_i), the velocity is fixed by the particle velocity. In principle, this procedure implies the violation of the local mass conservation in Eq. 7. Note that this is equivalent to applying a body force \mathbf{f}_{FDM} on the liquid:

$$\mathbf{f}_{FDM} = \rho_f \frac{\partial}{\partial t} (\hat{\mathbf{U}} - \mathbf{U}) \tag{8}$$

where $\hat{\mathbf{U}}$ is the new velocity field after fixing the velocities inside each node. As can be noticed, $\hat{\mathbf{U}}$ is not divergence-free. In order to keep the validity of the continuity equation, a corrected velocity field $\mathbf{U}^\dagger = \hat{\mathbf{U}} - \nabla \Phi$ is introduced. It guarantees that $\nabla \cdot \mathbf{U}^\dagger = 0$, and consequently:

$$\nabla \cdot \hat{\mathbf{U}} = \nabla^2 \Phi. \tag{9}$$

Table 1 Spatial and temporal resolutions for each set of experimental run. The point of contact $z = 0$ between sphere and wall is defined by the last position of the center of the particle subtracted by its radius. The resolution of this point is also available in the table

Material	Radius (mm)	FPS (frame/s)	Spatial resolution (pixel/mm)	Position Error (mm)	Precision of $z = 0$ (mm)
Steel	0.5	125	68	0.026	0.032
Steel	1.0	500	32	0.072	0.081
Steel	1.5	1000	24	0.110	0.180
Plastic	1.0	500	39	0.063	0.070

Finally, the Navier–Stokes equation is redefined considering $\hat{U} = U^\dagger + \nabla\Phi$:

$$\rho_f \frac{\partial U^\dagger}{\partial t} + (U \cdot \nabla)U = -\left(\nabla p + \rho_f \frac{\partial \nabla\Phi}{\partial t}\right) + \mu \nabla^2 U + \rho_f \mathbf{g} + \mathbf{f}_{FDM} \quad (10)$$

The technical description of the used numerical tool is in the literature [42]. However, no specific details about the implementation of the particle motion towards a wall is available.

The discrete element method (DEM) has the capacity to resolve the behavior of granular media at the particle scale [47]. In a typical DEM simulation, all the particles in the computational domain have their motion solved explicitly in every time step. Accordingly, the DEM is capable of simulating a wide variety of systems, from dense to dilute particulate systems, as well as rapid and slow granular flow. The general details of the used method are presented here, and a full description is provided by Goniva et. al. [47].

3.1 Simulation parameters

The simulation details are adjusted to achieve a good match between the calculation and experimental results. We simulate the motion of a sphere of radius $R = 1$ mm in a 3D viscous fluid. Particle and fluid densities are $\rho_p = 7.60$ g/cm³ and $\rho_f = 0.97$ g/cm³, respectively. The fluid has kinematic viscosity $\nu = 1000$ cSt. As per the experimental counterpart, we examine a sphere initially placed at the central position of the simulation domain, and we left it to settle from rest in a quiescent fluid. We set a grid resolution equal to $\Delta x = R/4$ and varying integration time steps Δt , which was kept the same for the CFD and DEM. For the sake of generality, the time steps are always referred to as a fraction of the characteristic time given by the stokesian dynamics in an unbounded fluid $\tau = \frac{2}{9\mu} \rho_p R^2$.

4 Results and discussions

4.1 Particle–wall collision in viscous fluid: unbounded case

We start by summarizing the relevant velocities and dimensionless numbers observed in our data. Table 2 lists the set of Stokes velocities (v_S) for each particle type, their respective observed terminal velocities (v^*), and their respective Reynolds ($Re = \frac{v^* 2R}{\mu}$) and Stokes ($St = \frac{1}{9} \frac{R_e \rho_p}{\rho_f}$) numbers. Note that the Stokes velocity and the dimensionless numbers were calculated using the experimental values described in Sect. 2. We observe that the measured terminal velocities (v^*) of the particles in all cases are below the 3% deviation from the Stokes velocity. It is also important to notice that

the Reynolds numbers are below 0.1 for all configurations, indicating creeping flow conditions for all runs. Lastly, the Stokes numbers indicate that no bouncing motion should be observed, considering the findings of Gondret et al. [11].

We proceed to describe the complete settling process for each particle inside the three used cells. These results are summarized in Fig. 3. In all cases, the data show similar trends, a long linear periods of time where the particle pass equal distances at equal time intervals, followed by a strong deceleration when approaching the wall. Note that no rebound is observed. The insets of all figures show the velocity v^*/v_S when varying the bead type and contrast the terminal velocity found with the expected Stokesian velocity. To compare the temporal evolution, we arbitrarily select the location $h_z = 3.5$ cm as the initial vertical coordinate, which correspond to $t = 0$ s. At this height, the space-time curves are linear, providing a straightforward way of calculating the particle terminal velocity, corresponding to each confinement, v^* . As mentioned earlier, a cube with $10 \times 10 \times 10$ cm is used to mimic the infinite size limit (see Fig. 3a). In this particular case, the slope of the linear fit should match the stokesian limit, providing an excellent baseline to compare the effects of the lateral confinement on the asymptotic velocity. The inset in Fig. 3a illustrates the values of terminal velocities, obtained for the four studied types of beads. Remarkably, our measurements reproduces stokes' terminal velocity with excellent accuracy.

Nevertheless, the use of narrower cells (increasing the lateral confinement) implies a systematic decrease of the terminal velocity, as clearly depicted by the insets of Fig. 3b, c. In fact, it is the reflex of the influence of the lateral walls, which increase the drag force and, as a result, the limit velocity v^* reached by the particles decreases significantly. We rationalize our experimental findings of v^* using the expression introduced by Haberman and Sayre [see Eq. (3)]. They considered a spherical particle falling along the axial direction of a long cylindrical container, assuming the same cylindrical boundary conditions for both the particle and the container wall. In our case, the squared corners could have an influence on the particle, although we compare the experimental results with the parameter K introduced in [21]. We assume that an effective radius, $R_w = \frac{W}{\sqrt{\pi}}$, can be estimated from the container section, W^2 . As is evident from the continuous line in Fig. 4, this first-order approximation allows us to describe the influence of square-section containers. Note, it resembles a symmetric drag acting on the particle due to a cylindrical container of radius R_w .

After examining the role of the lateral confinement on the asymptotic limit velocity of the particle, let us concentrate on the influence of the bottom wall on the particle velocity. Figure 5 summarizes the main features obtained experimentally using a cube with $10 \times 10 \times 10$ cm. For the sake of

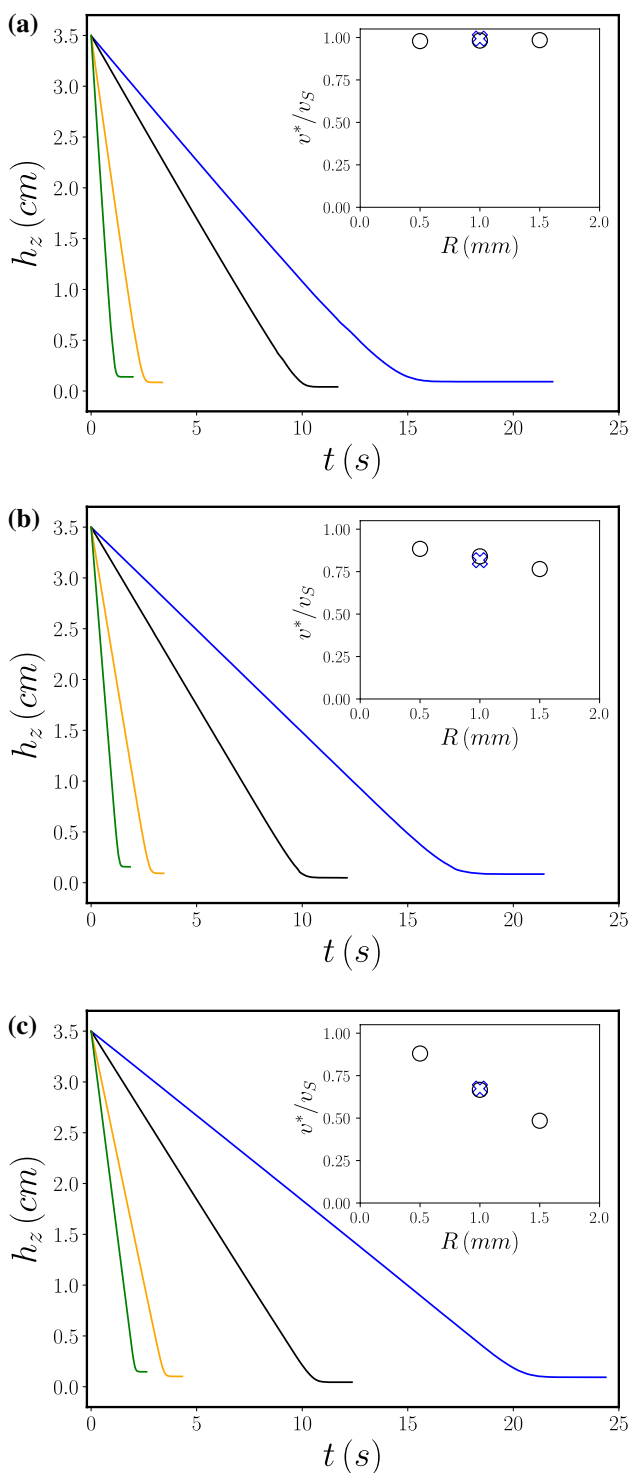


Fig. 3 Experimentally observed trajectories of the settling of different spheres in a viscous fluid. Outcomes corresponding to different particle radius and containers are presented. Data corresponding to the containers **a** $W = 10$ cm, **b** $W = 2$ cm, and **c** $W = 1$ cm. The colors indicate: $R = 1.5$ mm (green), $R = 1.0$ mm (yellow), $R = 0.5$ mm (black), and plastic $R = 1.0$ mm (blue). In the insets, we observe the velocity v^*/v_S when varying the type of bead used. The steel spheres are represented by black circles and the plastic spheres by blue crosses

generality, the case of two different materials (steel and plastic) and various particle radii are examined. As mentioned earlier, the no border scenario has been handled analytically (see Brenner’s approximation in Sect. 1), and it will serve as a baseline to investigate confined cases. The results show that the larger the bead mass, the shorter the time necessary to reach the bottom. Hence, the numerical integration of Brenner’s approach (using a drag force given by Eq. (4)) provides an excellent agreement with the measured positions when setting the initial numerical conditions from the experimental ones.

The long-range effect induced on the particle dynamics by the bottom wall is more clearly evidenced in the panels of Fig. 5d-f), where particle velocities are displayed against the vertical distance $z = h_z - R$. In all cases, velocity variations are perceptible for distances larger than ten times the particle radius. Moreover, the sphere reaches the wall with practically zero velocity, and no bouncing motion is observed. These panels also suggest that results can be collapsed using adequate kinetic and spatial scales. Assuming that the theoretical Stokes’s velocity v_S is the characteristic velocity scale in this case, Fig. 6 shows the collapse obtained when the dimensionless velocity is plotted against the normalized gap distance z/R to the bottom-wall. The black solid line represents the numerical integration of Brenner’s drag force given by Eq. (4), considering the initial condition as the terminal velocity at $z = 20R$. Note that regardless of the particle size or density, the resulting behavior is compatible with the scaled Brenner’s approximation (see Eq. (5)), and Brenner’s theoretical framework fully describes the characteristic motion of the particle towards the wall.

Until here, our outcomes deliver two main messages. Firstly, the experimental procedure can measure the particle-wall collision with great accuracy and repeatability. Besides, the results obtained using a large cube reproduce the theoretical limit of particle-wall collisions under creeping flow conditions.

4.2 Particle-wall collision in viscous fluid: confined conditions

Provided a reference baseline for the particle-wall collision process, we repeat the experiment but using narrower containers. Our aim is to clarify the impact of confinement on the collision dynamics.

In Fig. 7a, we show the time evolution of the velocity of particles settling and colliding while subjected to lateral confinement. The figure compares outcomes obtained for spheres with different radii and density but subjected to the same level of confinement. Specifically, two different steel beads with radius $R = 0.5$ mm and $R = 1.0$ mm and a plastic bead $R = 1.0$ mm are tested. In all cases, the confinement is

Table 2 Velocities and dimensionless numbers for the set of experimental configurations used

Material	Radius (mm)	v_S (cm/s)	v^* (cm/s)	Reynolds number	Stokes Number
Steel	0.5	0.37	0.37	0.0036	0.0286
Steel	1.0	1.49	1.46	0.0293	0.2292
Steel	1.5	3.35	3.30	0.0990	0.7756
Plastic	1.0	0.247	0.245	0.0049	0.0385

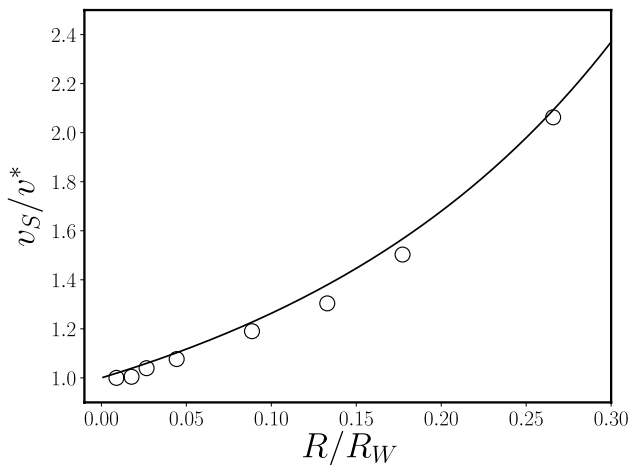


Fig. 4 The additional drag force acting on the particle v_S/v^* versus the relative confinement R/R_W . It shows a good agreement between the expression introduced by Haberman (black line) and the experimental results [21]

the same with $W = 20R$. As can be appreciated in Fig. 7a, we detect a steady-state regime characterized by a well-defined terminal velocity v^* , which depends strongly on the particle size and density. Similarly to the results obtained for $W = 100R$, the particle gets close to the wall, and its velocity diminishes practically to zero at the final stage. The corresponding spatial dependencies of the particle velocity are illustrated in Fig. 7b. For convenience, the data is rescaled using the particle radius R and the obtained terminal velocity v^* , as characteristic scales, respectively. Interestingly, the data collapse suggests that the beads approach the wall experiencing the same energy loss mechanisms, regardless of their size and material. However, the behavior illustrated in Fig. 7b is not compatible with Brenner’s formulation [16], indicated by the red curve and the terminal velocity $v^* = v_S$. This incompatibility is observed in the full domain of the distance from the wall.

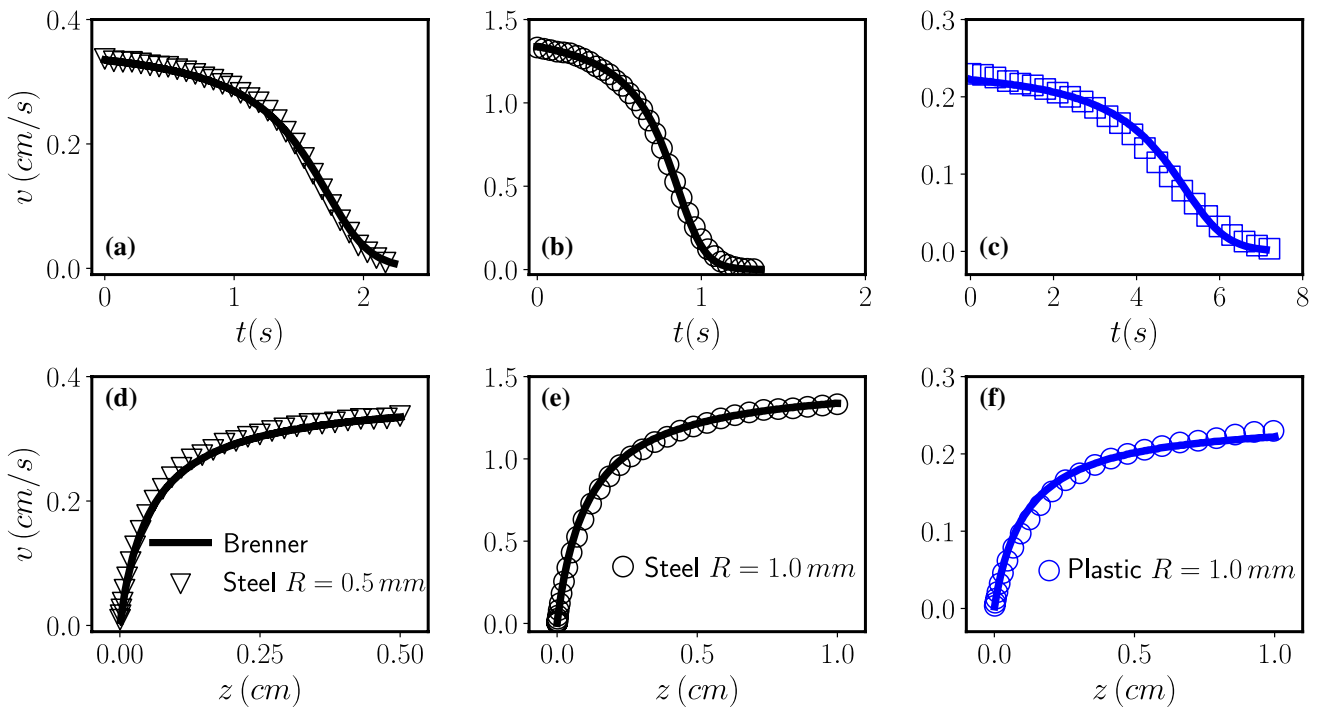


Fig. 5 a–c Experimental velocity v as a function of time for $R = 0.5$ mm, **b** $R = 1.0$ mm, and plastic $R = 1.0$ mm beads settling in the container with $W = 10$ cm. **d–f** The experimental velocity v as a

function of the gap to the wall z . In all cases, the solid lines represent the analytical solution of Eq. (1) predicting the particle motion

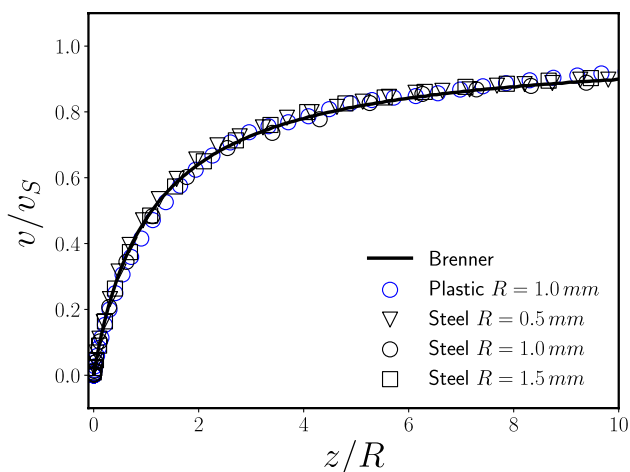


Fig. 6 Experimental velocity v/v_S with respect to the gap z/R for four different beads of different radius and density, settling in the acrylic cube. The black solid line represents the analytical solution of Eq. (1) corresponding to the particle motion

Next, our efforts focus on clarifying how different levels of confinement affect the collision dynamics of the beads. Figure 8a illustrates the time evolution of the velocity of a sphere of $R = 1.0$ mm sedimenting towards a wall under different confinements $W = [10R, 20R, 100R]$. As mentioned earlier, the confinement significantly affects the limit velocity of the particle. Moreover, it also influences the collision dynamics, determining the instants of time when the wall effect is significant, and when impact occurs.

Complementarily, Fig. 8b analyzes the data but rescaled using the particle size R and the Stokesian settling velocity v_S , as the characteristic size and velocity scales respectively. For comparison, Brenner’s theoretical formulation [16] is also included. The collapse in the data indicates that at locations $z < R$ the particles experience an energy loss mechanism which is compatible with Brenner’s theoretical formulation. However, a distinct behavior is identified beyond a particular spatial scale. Initially, the particle maintains a constant limit velocity v^* which is abruptly reduced. Consequently, Fig. 8b shows that the data corresponding to $W \leq 20R$ is not compatible with Brenner’s formulation at large distances from the wall.

In general, we observed that this critical distance depends on the confinement strength, but it is comparable with the particle size in all cases. Thus, the obtained trends indicate that increasing the confinement level reduces the typical length scale where the drag experienced by the particle depends on the location of the bottom wall. We can argue that Brenner’s approach fails in these cases ($W \leq 20R$), because by its construction the expansion $\lambda(h_z)$ (see Eq.(5)) only imposes the particle radius R as the characteristic length of the creeping particle as it decelerates to

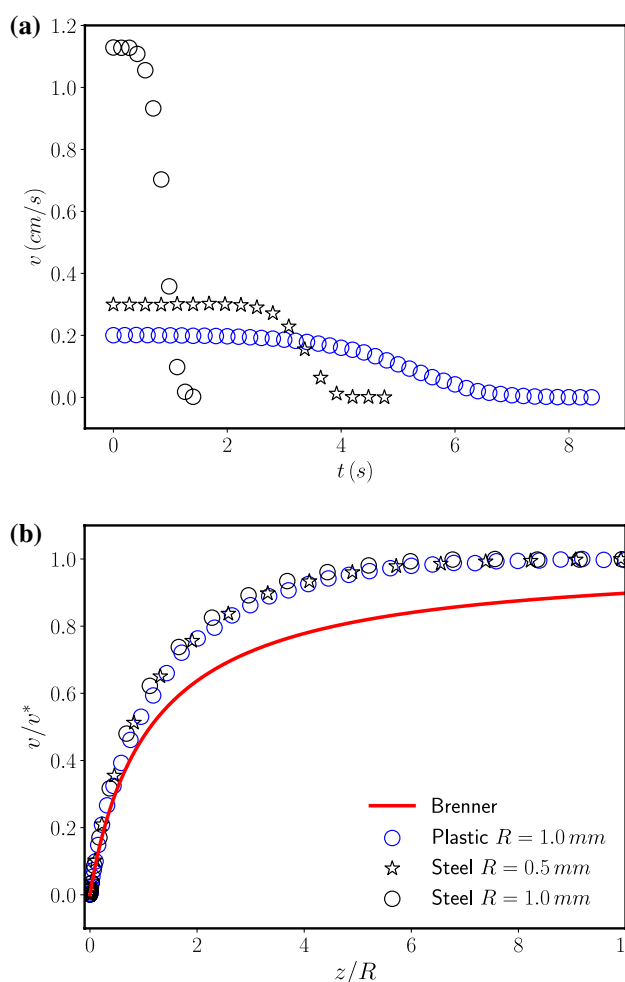


Fig. 7 **a** Experimental temporal evolution of the velocity v for beads subjected to the same confinement of $W = 20R$ with different radii and materials. **b** Experimental velocity v/v^* as a function of the gap z/R . In all cases, the relative behavior only depends on the relative confinement

zero velocity, in the neighborhood of the wall. As a result, Brenner’s formulation predicts a smooth decreasing in the particle velocity from the Stokesian limit, which is at infinite distance from the bottom wall. As we commented earlier, our outcomes indicate this assumption can also be made in the (quasi) unbounded limit with $W = 100R$ (see Fig. 6). However, even considering the boundary correction that accounts for the confinement effect [16], the experimental data corresponding to confined conditions is not reproduced. In all cases, we detect a finite length where the bottom wall influence almost disappears. It is worth mentioning that equivalent results are obtained using plastic beads (data not shown), which confirm the validity of our analysis.

We speculate that this sudden evolution is related to changes in the transient hydrodynamic force exerted on the particle by the advected fluid. In Sect. 4.4, the numerical

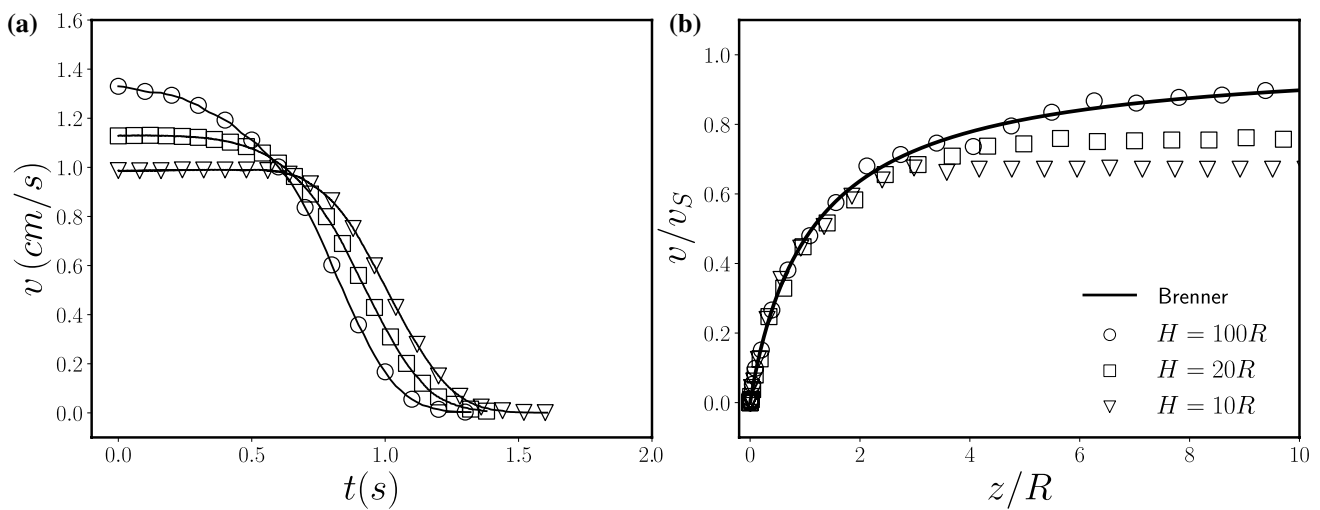


Fig. 8 **a** Experimental velocity v as a function of time for a $R = 1$ mm steel bead settling in three containers with different width. **b** Experimental velocity rescaled with the Stokesian settling velocity v/v_S with

respect to the gap z/R . The black solid line is the solution of the Eq. (1) considering the force given by Eq. (4)

approach demonstrates that the lateral confinement induces notable changes in the advected fluid dynamics around the sphere. Consequently, the proper dynamic analysis to describe the particle movement would require the integration of the momentum balance equation using the correct set of boundary conditions for the particle and walls. Although this is beyond the scope of our research, next we introduce a simple scaling analysis, shedding light on the relevant scale of this problem.

On the one hand, note that although the unbounded regime can be rendered dimensionless by assuming v_S and R as typical scales, it is not valid for confined systems. On the other hand, Fig. 8a shows that the larger the initial velocity, the larger the deceleration involved in the collision due to the time necessary to reach the bottom being smaller. Therefore, based on simple dimensional analysis, we propose a typical length scale for the collision process as $\zeta \sim (v^*)^2/a_c$, where a_c accounts for the particle acceleration during the collision process. In each case, we derive the specific values of a_c and v^* from the experimental data. Figure 9 shows the collapse of all the data corresponding to confined conditions into a single master curve when using ζ and v^* as relevant distance and velocity scales, respectively. Remarkably, the analysis holds for particles of different sizes and materials. For comparison, Fig. 9 also includes the outcome obtained for the unbounded limit, denoting a different characteristic scale. This shows that the particle-wall collisional scale is influenced by the level of confinement, and the length scale $\zeta \sim (v^*)^2/a_c$ governs the strength of the effective interaction between the particle and bottom wall.

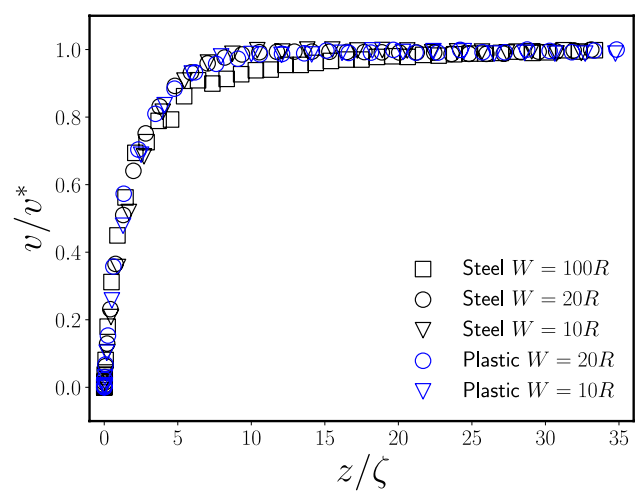


Fig. 9 Experimental v/v^* vs the scale-free distance z/ζ for different confinements and materials. Experimental results for the confined scenarios to steel and plastic are represented with black and blue circles, respectively

4.3 Numerical confined collisions

As first step and guided by our experimental findings, we assess the capabilities of the used numerical method. It also allows us to enrich the analysis, exploring the fluid dynamics involved in the drag process. Thus, we perform simulations to mimic the explored confinements. However, due to computing limitations (running time and memory limits), the widest system investigated has $W = 20R$ wide. Specifically, we simulate a steel particle with radius $R = 1.0$ mm settling

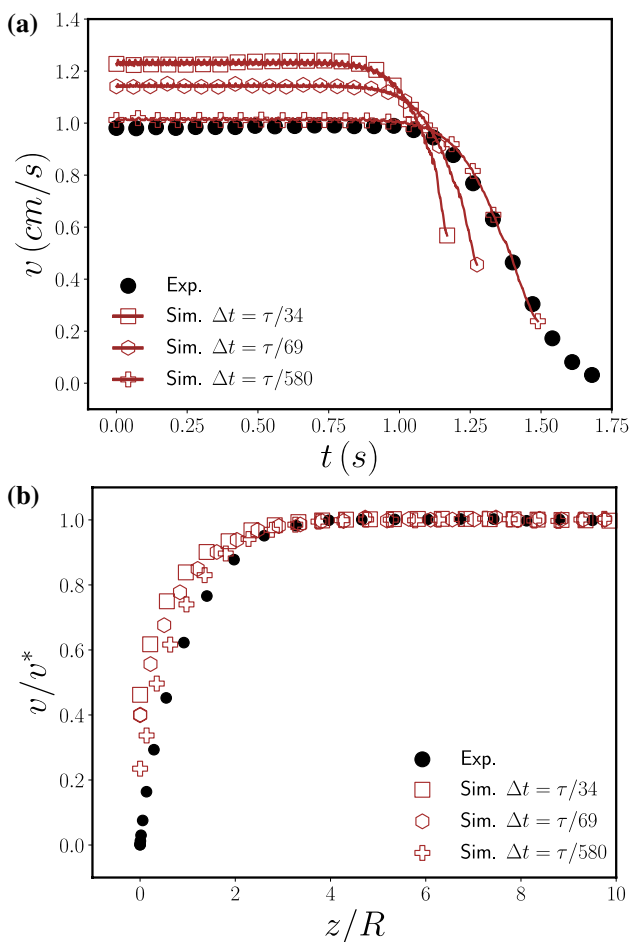


Fig. 10 **a** Numerical velocity v vs. time t for different time steps with fixed confinement $W = 10R$. **b** Velocity v/v^* versus gap z/R for a confined system with $W = 10R$. The particles radius is $R = 1.0$ mm, in all cases. The black circles represent the experimental values, while the colored ones represent the numerical results for different time steps

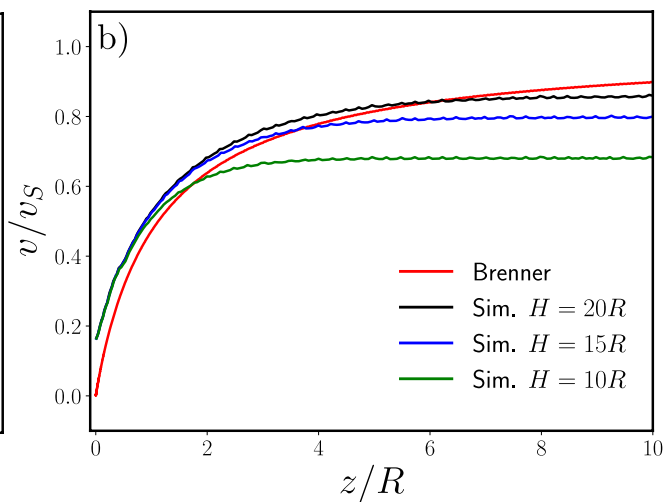
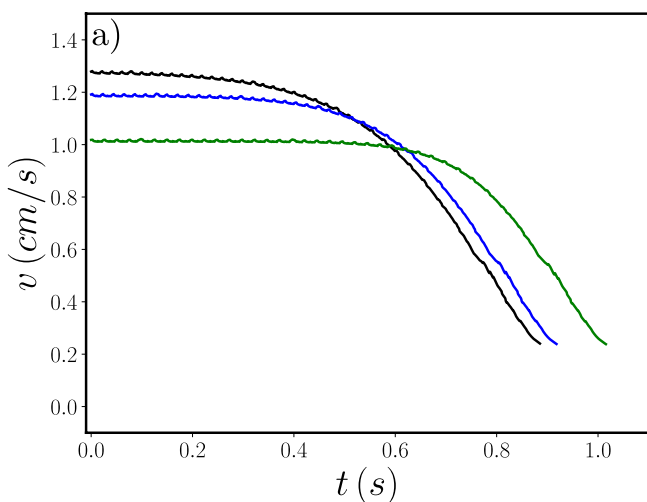


Fig. 11 **a** Numerical velocity v as a function of time for a $R = 1$ mm bead settling in three containers with different widths. **b** Numerical velocity v/v_s with respect to the gap z/R . The red solid line is the

into squared-section boxes with lateral dimension: $W = 20R$, $W = 15R$ and $W = 10R$.

Figure 10a) illustrates the evolution in time of the bead velocity settling in the $10R \times 10R \times 30R$ box. For validation purposes, the figure illustrates results obtained for several time steps Δt , and the same spatial discretization $R/4$. In addition, the corresponding experimental data (black circles) is included for comparison. As expected, the motion of the particle towards the wall is better resolved as the integration time step is reduced, yielding more realistic impact length and collision velocities. Besides, Fig. 10b) portrays the obtained spatial evolution of the velocity v in terms of the limiting velocity v^* . The outcomes indicate the used numerical tool describes the complete deceleration process with reasonable accuracy. However, in all cases, we obtain that the particle reaches the wall with non-zero velocity. This discrepancy is related with both the finite discretization of the fluid representative volume element and the integration time step. Indeed, the application of lubrication theory might be needed to compensate for the lack of spatial resolution in the simulations [17, 18]. Altogether, we evaluate the capability of the numerical tool, varying the integration time step; and finding it is conditioned by a time step lower than $\tau/580$. In that conditions, the used CFD-DEM method reproduces with reasonable accuracy the motion of spheres moving toward a wall under confined conditions. The trend suggests that an infinitely small-time and space discretization would reproduce the experimental results.

After adjusting the parameters of the numerical model, we systematically analyze the particle dynamic changing the confinement conditions. Figure 11a) displays the temporal evolution of the vertical velocity, as the particle approaches to the bottom-wall. For comparison, outcomes of three different confinements are illustrated $W = [10R, 15R, 20R]$. As

solution of the Eq. (1) considering the force given by Eq. (4). For all numerical results presented, the integration time step used was $\Delta t = \tau/580$

expected, the limit velocity is strongly affected by the lateral dimensions of the box. Moreover, the confinement strength also affects the collision dynamics, determining the instant at which the wall effect is significant. However, as we pointed out earlier, the numerical tool fails in accurately determining the moment when impact occurs. Figure 11b shows the spatial dependency of the particle's velocity. Similarly to the experimental analysis (see Fig. 8b) we use the particle size R and the Stokesian settling velocity v_S as the characteristic scales. The outcomes are compared with Brenner's theoretical formulation [16]. Note that in the region close to the wall with $z < R$, we obtain a collapse in the data, but it deviates from Brenner's formulation. However, as in the experimental case, we find that the larger the confinement is, the smaller the typical distance where the bottom-wall drag influences the particle dynamics. Thus, Brenner's creeping stationary solution does not capture the rapid change of the particle velocity from its asymptotic value.

Next, we replicate the experimental data processing, do a simple dimensional analysis, and propose a typical length scale of the collision process as $\zeta \sim (v^*)^2/a_c$, where a_c accounts for the particle acceleration and v^* is the measured limit velocity. The values of a_c and v^* are directly obtained from the numerical tool. Remarkably, Fig. 12 illustrates the collapse in the data corresponding to three confined values $W = [10R, 15R, 20R]$ into a master curve with ζ and v^* as relevant distance and velocity scales respectively. Thus, the CFD numerical tool reproduces the result that the level of confinement influences the particle-wall collisional scale. Furthermore, the length scale $\zeta \sim (v^*)^2/a_c$ seems to govern the strength of the effective interaction between the particle and bottom wall. Notably, the numerical approach is capable of reproducing the main features of the bead dynamics.

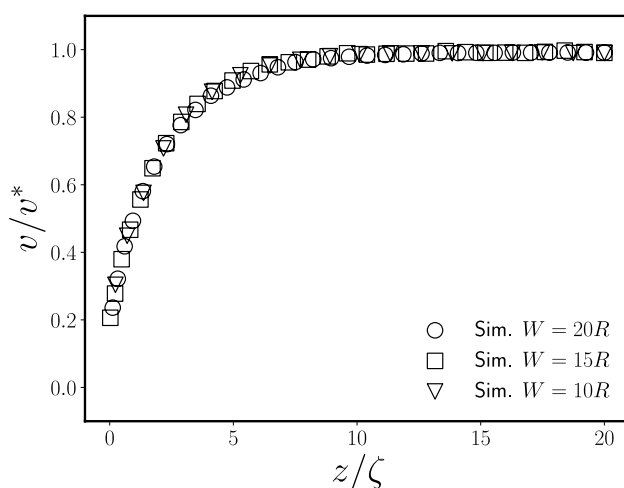


Fig. 12 Numerical data for v/v^* vs the scale-free distance z/ζ for different confinements. For all numerical results presented, the integration time step used was $\Delta t = \tau/580$

In the next section, we extract relevant information of the CFD results about the role played in the settling process by the fluid dynamics around the bead, and the fluid-wall interaction.

4.4 Response of the fluid phase

Numerical simulations allow us to obtain valuable information about the motion of the fluid and the stresses it experiences as the particle moves through it. Next, we illustrate the velocity fields (U_x and U_z) and pressure fields (p^k) obtained in the conditions mentioned above.

Figure 13 shows the streamlines for the velocity field U corresponding to the systems with two confinement levels $W = 20R$ and $W = 10R$, respectively. In both cases, the analysis focuses on the cell corresponding to the central plane, where the particle moves through during the settling process. The figure displays the velocity fields in the $x - z$ plane, and the particle position. The first two panels (a) and (b) show the fields after the particle reaches its asymptotic velocity. A symmetrical pattern develops as the particle settles. Besides, this pattern remains while the particle is at a distance large enough from the bottom wall denoting steady-state conditions. In the unbounded case, it is known that the streamlines of the disturbance velocity field typically converge above the particle and diverge below. Moreover, at a large distance from the particle, the flow lines are parallel to each other. However, as noticed in Fig. 13, the presence of the lateral walls induced almost symmetric vortical structures accompanying the particle displacement. This vortex enhances energy dissipation, and consequently, the effective drag is larger than the Stokesian limit expected without boundary conditions. Thus, the numerical results show that the development of a well-structured vortex correlates with increasing the momentum transmission towards the lateral walls. As the particle gets closer to the bottom wall, the vortex rings are markedly disturbed. Systems with low confinement develop large vortical currents, which interact earlier with the bottom wall, reducing the efficiency of the momentum transmission to the lateral wall by increasing the stress transmission to the bottom wall. The panels in the second row (c) and (d) of Fig. 13 show the ring structure at $z/R = 5$. The system with $W = 20R$ has already perturbed streamlines, while for the case $W = 10R$, it is still invariant despite the presence of the bottom wall at the same distance.

In both cases, the graphs also show that the outward motion of the fluid with respect to the particle vanishes as the sphere approaches the bottom wall. Nevertheless, the region perturbed by the vortex deformation is larger as the confinement is small, but in a larger confinement situation the displaced liquid and its influence is strongly restricted to the surrounding of the particle. Hence, in less confined systems, the intensity of the bottom-wall dissipation is

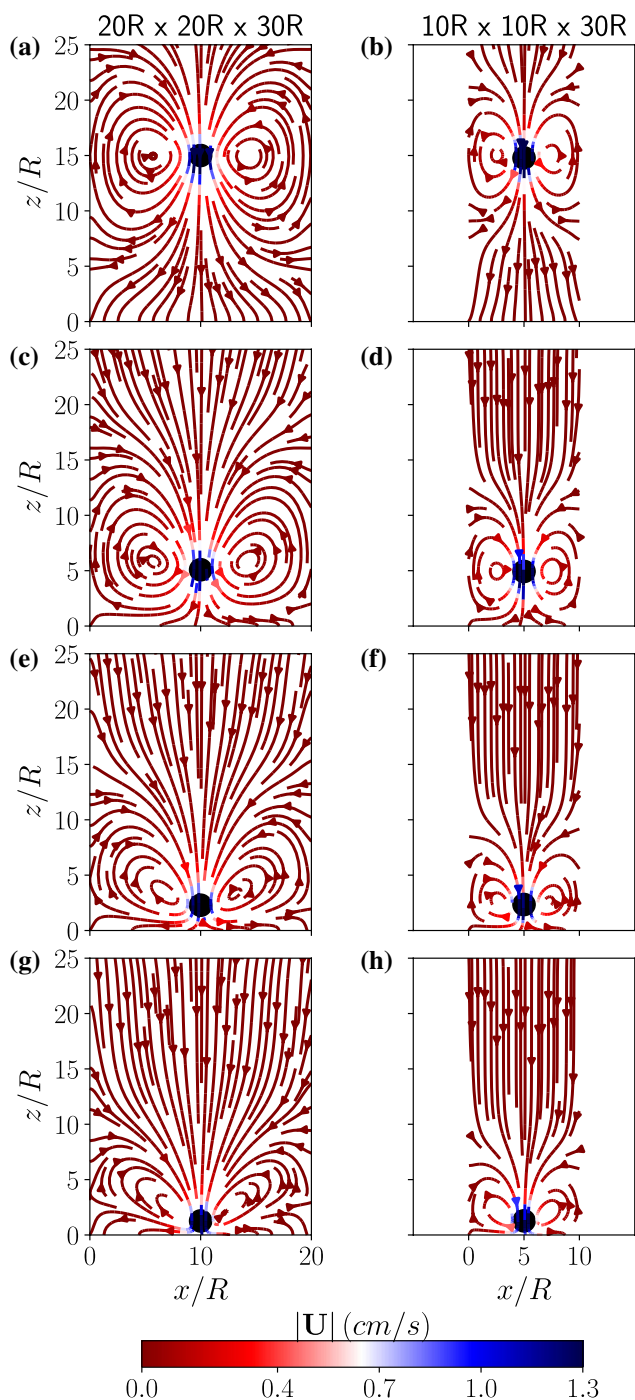


Fig. 13 Streamlines for the velocities fields for the systems with $W = 20R$ and $W = 10R$, respectively. Both simulations were performed with a fixed integration time step $\Delta t = \tau/580$. The four frames shown represent **a, b** The moment when the particles reach their terminal velocities. **c–f** The moment when symmetry breaks and the total drag acting on the particle is now impacted by the presence of the bottom wall, for systems with $W = 20R$ and $W = 10R$, respectively, **g, h** the instant before the collision when the lateral circulation occurs in a reduced region with smaller intensity

restricted to a region not larger than the particle size, while in the more confined system, the opposite is true.

In order to further analyze the liquid fields, we implement the spatio-temporal diagrams showed in Fig. 14. These diagrams provide an insight into the temporal evolution of the horizontal profiles U_x and U_z . In the diagrams, the temporal evolution has been replaced by its corresponding vertical coordinate to compare to the previous results directly. Thus, it is easy to distinguish this case as the fluid vertical velocity rapidly decreases beyond the particle limit and eventually inverts its direction (see Fig. 14a), until the magnitude becomes zero near the lateral wall. The strength of the energy dissipation will be associated with the spatial gradient of U_z , which becomes more relevant as the confinement is increased. However, this mechanism seems not to be strongly affected by the bottom wall until $h < d$ as can be concluded from Fig. 14b where U_z profile is normalized with respect to the corresponding particle velocity.

The temporal evolution of the horizontal velocity gives us more relevant information. In this case, we consider the U_x profile located at a distance z (the lower extreme of the bead). Contrary to the former situation, this profile changes when the particle reaches a vertical distance similar to the particle size. Note that the magnitude of the spatio-temporal evolution (normalized with respect to the corresponding vertical velocity) indicates that the peak of the horizontal velocity becomes almost equal to one, i. e., the dissipation at the collision is controlled by the wall boundary layer dissipation instead of the vortical circulation.

Additionally, we assess the spatial stress profile acting on the fluid, evaluating the kinetic pressure field p^k . Figure 15 illustrates the p^k fields corresponding to same representative configurations of particle displacements. The first two panels (a) and (b) show the p^k spatial profiles obtained when the particle reaches its terminal velocity at ($z/R = 15$) and at $z/R = 5$. Both situations are comparable with each other, with almost symmetric isobaric profiles. Moreover, at the depth where U_x starts to grow, the profiles become asymmetric, and the bottom wall influence is evident. A pressure gradient from the bottom wall towards the particle starts developing at this stage, indicating the characteristic distance at which the bottom wall begins affecting the particle motion.

The over-pressure generated by the bottom wall causes the fluid horizontal velocity responsible for the energy dissipation at the final stages of the collision. Remarkably, at that stage, the pressure gap between the particle and the bottom wall is one order of magnitude larger than the values when the sphere was far from the wall. During the deceleration process, the numerical method is capable of approximately

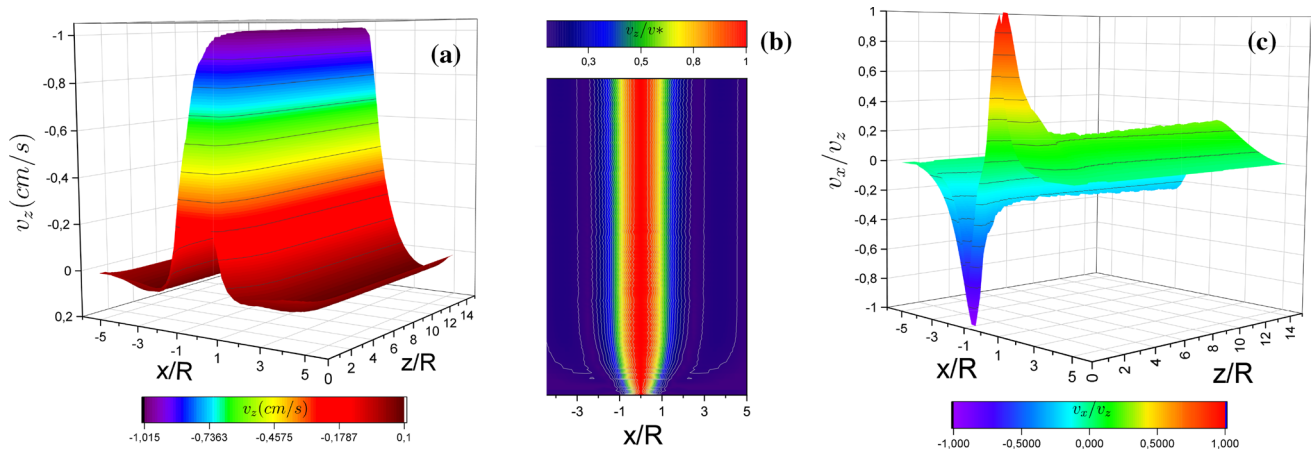


Fig. 14 Spatio-temporal diagrams of the velocity fields **a** U_z and **c** U_x for a system with width $W = 10R$ as the sphere moves towards the bottom wall. The contour lines of **a** are represented in **(b)**. The slice

taken of the z -axis is considered to represent the general patterns found around the particle and we can represent its changes over time. The integration time step used was $\Delta t = \tau/580$

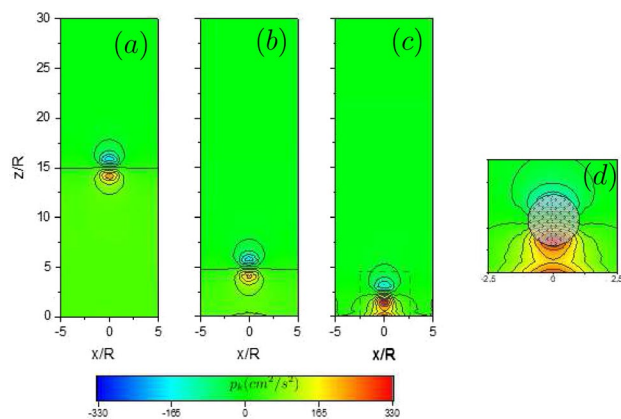


Fig. 15 Kinetic pressure (p_k) for the systems with $W = 10R$. **a** The instant when the particle reaches its terminal velocity. **b** The moment when the influence of bottom wall starts to impact the motion of the particle. **c** The moment when the spheres reaches $h_z = 2R$. **d** represents a close-up look around the sphere for the frame in **(c)**. The integration time step used was $\Delta t = \tau/580$

resolving the motion of the particle according to the experimental results (refer to Fig. 10). However, the particle reaches the bottom wall with a non-zero velocity, indicating that it does not fully reproduce the typical drag force acting on the particle. These outcomes seem to indicate that the pressure values represented in the last two panels in Fig. 15 are underestimated when compared to the expected in the experimental scenario.

The results discussed in the present section reveal four features of the dynamics inside the simulated domain. Firstly, a vortex ring circulation occurs, driven by a pressure gradient caused by the sphere movement and the presence of the lateral walls. Secondly, a pressure gradient develops from the bottom wall and particle when the particle approaches

the wall. This gradient increases when the gap distance decreases and the particle experiences a more significant drag force. Thirdly, the degree of confinement determines the upstream flow in the lateral walls, implying that more kinetic energy is present in the region between the surface of the particle and the wall for highly confined particles. Lastly, the outward motion of the fluid with respect to the particle grows when the sphere approaches the bottom surface, this effect is not captured by the vortex dynamics (see Fig. 13) as evidently observed from Fig. 14c).

Summarizing: we examine experimentally and numerically the behavior of solid macroscopic spheres when settling from rest in a fluid toward a solid wall under confined and unconfined situations. The experiments are done using particles of two different materials and several sizes. The particle trajectories are accurately measured using a high-speed digital camera. Interestingly, the particle deceleration is typically observed at distances larger than ten diameters of the particle from the wall, regardless of the confinement imposed. Although all the explored scenarios lead to collisions with zero velocity, a noticeable difference is reported in how the deceleration occurs. For unconfined configurations, our findings are in excellent agreement with well-established analytical frameworks, used to describe the forces acting on the sphere. Besides, the experimental values of the terminal velocity obtained for different confinements are also in very good agreement with previous theoretical formulations. Similar conditions are simulated using a resolved CFD-DEM approach. After adjusting the parameters of the numerical model, we analyze the particle dynamic under several confinement conditions. The simulations results are contrasted with the experimental findings, obtained a reasonable agreement.

We analyze large systems varying the radius of the bead and show the excellent agreement of our results with the analytical solution provided by Brenner. However, the results indicate that confined particles have different dynamics responses as they approach the bottom wall, and their motion cannot be described by the analytical solution introduced for the infinite system. Indeed, the confinement strongly affects the spatial scale where the particle is affected by the bottom-wall and, accordingly, the dimensionless results can not be collapsed in a single master curve using the particle radius as the typical scale. Alternatively, we rationalized our findings using a simple dynamical approximation, explaining a particle's deceleration process while approaching a flat wall. Accordingly, a confinement-dependent spatial scale allows us the collapse of the data (see Fig. 9), revealing the typical distance at which the bottom wall influences the particle displacement under confinement conditions. Furthermore, we expect that this scaling analysis will also be valid to describe bead-to-bead collisions. Hence, the clogging probabilities described in a series of recent papers that study the passage of particles through constrictions could be affected by confinement level as the relative particle velocity is notably affected by the confinement [48].

Finally, the numerical simulations also allow us to obtain valuable information about the motion of the fluid and the stresses it experiences as the particle moves through it. The evolution of the fields indicate the apparition of vortex ring circulations, which are caused by the sphere movement and the presence of the lateral walls. As a result, a pressure gradient develops from the bottom wall, increasing when the gap distance decreases. These outcomes strongly suggest that the degree of confinement determines the upstream flow in the lateral walls, implying that more kinetic energy is present in the region between the surface of the particle and the wall for highly confined particles.

Acknowledgements We would like to thank Luis Fernando Urrea for all technical support provided during the experiments. This work has been partially supported by Fundación Universidad de Navarra and Ministerio de Economía y Competitividad (Spanish Government) Projects No. FIS 2017-84631 and PID2020-114839GB-I00, MINECO/AEI/FEDER, UE. I. Fonceca also thanks Asociación de Amigos de la Universidad de Navarra for his scholarship.

Funding Open Access funding provided thanks to the CRUE-CSIC agreement with Springer Nature.

Declarations

Conflict of interest The authors declare that they have no conflict of interest, and the work is original and have not been published elsewhere in any form or language.

Open Access This article is licensed under a Creative Commons Attribution 4.0 International License, which permits use, sharing, adaptation, distribution and reproduction in any medium or format, as long as you give appropriate credit to the original author(s) and the source, provide a link to the Creative Commons licence, and indicate if changes were made. The images or other third party material in this article are included in the article's Creative Commons licence, unless indicated otherwise in a credit line to the material. If material is not included in the article's Creative Commons licence and your intended use is not permitted by statutory regulation or exceeds the permitted use, you will need to obtain permission directly from the copyright holder. To view a copy of this licence, visit <http://creativecommons.org/licenses/by/4.0/>.

References

1. Truskey, G., Yuan, F., Katz, D.: *Transport Phenomena in Biological Systems*. Pearson Prentice Hall, Hoboken (2004)
2. Happel, J., Brenner, H.: *Low Reynolds Number Hydrodynamics*. Martinus Nijhoff Publishers, Leiden (1983)
3. Batchelor, G.: A new theory of the instability of a uniform fluidized bed. *J. Fluid Mech.* **193**, 75–110 (1988)
4. Di-Carlo, D., Edd, J., Humphry, K., Stone, H., Toner, M.: Particle segregation and dynamics in confined flows. *Phys. Rev. Lett.* **114**, 094503 (2009)
5. Nott, P., Brady, J.: Pressure-driven flow of suspensions: simulation and theory. *J. Fluid Mech.* **272**, 157–199 (1994)
6. Fall, A., Lemaître, A., Bertrand, F., Bonn, D., Ovarlez, G.: Shear thickening and migration in granular suspensions. *Phys. Rev. Lett.* **105**, 268303 (2010)
7. Amini, H., Sollier, E., Weaver, W., Di-Carlo, D.: Intrinsic particle-induced lateral transport in microchannels. *Proc. Natl. Acad. Sci. USA* **109**, 11593–11598 (2012)
8. Lee, W., Amini, H., Di-Carlo, D.: Dynamic self-assembly and control of microfluidic particle crystals. *Proc. Natl. Acad. Sci. USA* **107**, 22413–22418 (2010)
9. Mordant, N., Pinton, J.: Velocity measurement of a settling sphere. *Eur. Phys. J. B* **18**, 343–352 (2000)
10. Ambari, A., Gauthier-Manuel, B., Guyon, E.: Wall effects on a sphere translating at constant velocity. *J. Fluid Mech.* **149**, 235–253 (1984)
11. Gondret, P., Lance, M., Petit, L.: Bouncing motion of spherical particles in fluids. *Phys. Fluids* **14**, 643–652 (2002)
12. ten Cate, A., Nieuwstad, C.H., Derksen, J.J., Van den Akker, H.E.A.: Particle imaging velocimetry experiments and lattice-Boltzmann simulations on a single sphere settling under gravity. *Phys. Fluids* **14**(11), 4012 (2002)
13. Mongruel, A., Lamriben, C., Yahiaoui, S., Feuillebois, F.: The approach of a sphere to a wall at finite Reynolds number. *J. Fluid Mech.* **661**, 229–238 (2010)
14. Hagemeier, T., Thévenin, D., Richter, T.: Settling of spherical particles in the transitional regime. *Int. J. Multiphas. Flow* **138**, 103589 (2021)
15. Lorentz, H.A.: *Abhandlungen uber theoretische Physik*, vol. 1 (1907)
16. Brenner, H.: The slow motion of a sphere through a viscous fluid towards a plane surface. *Chem. Eng. Sci.* **16**, 242–251 (1961)
17. Li, Q., Abbas, M., Morris, J.F.: Particle approach to a stagnation point at a wall: viscous damping and collision dynamics. *Phys. Rev. Fluids* **5**, 104301 (2020)
18. Li, Q., Abbas, M., Morris, J.F., Climent, E., Magnaudet, J.: Near-wall dynamics of a neutrally buoyant spherical particle in

- an axisymmetric stagnation point flow. *J. Fluid Mech.* **892**, A32 (2020)
19. Bhattacharya, S., Blawdziewicz, J., Wajnryb, E.: Hydrodynamic interactions of spherical particles in suspensions confined between two planar walls. *J. Fluid Mech.* **541**, 263–292 (2005)
 20. Swan, J., Brady, J.: Particle motion between parallel walls: hydrodynamics and simulation. *Phys. Fluids* **22**, 103301 (2010)
 21. Haberman, W., Sayre, R.: Model basin report No. 1143. U.S. Navy Department (1958)
 22. Mongruel, A.: Boundary conditions for creeping flow along periodic or random rough surfaces: experimental and theoretical results. *J. Phys. Conf. Ser.* **392**, 012010 (2012)
 23. Despeyroux, A., Gauthier-Manuel, B., Guyon, E.: Direct measurement of tube wall effect on the Stokes force. *Phys. Fluids* **28**, 1559 (1985)
 24. Lecoq, A., Masmoudi, K., Anthore, R., Feuillebois, F.: Creeping motion of a sphere along the axis of a closed axisymmetric container. *J. Fluid Mech.* **585**, 127–152 (2007)
 25. Mongruel, A., Lecoq, N., Wajnryb, E., Cichocki, B., Feuillebois, F.: Motion of a sphero-cylindrical particle in a viscous fluid in confined geometry. *Eur. J. Mech. B-Fluids* **30**(4), 405 (2011)
 26. Despeyroux, A., Ambari, A.: Slow motion of a sphere towards a plane through confined non-Newtonian fluid. *J. Non-Newton. Fluid* **167–168**, 96 (2011)
 27. Souzy, M., Zuriguel, I., Marin, A.: Transition from clogging to continuous flow in constricted particle suspensions. *Phys. Rev. E* **101**, 060901 (2020)
 28. Campbell, A., Haw, M.: Jamming and unjamming of concentrated colloidal dispersions in channel flows. *Soft Matter* **6**, 4688 (2010)
 29. Agbangla, G.C., Bacchin, P., Climent, E.: Collective dynamics of flowing colloids during pore clogging. *Soft Matter* **10**, 6303 (2014)
 30. Laar, T.V.D., Klooster, S.T., Schroen, K., Sprakel, J.: Transition-state theory predicts clogging at the microscale. *Sci. Rep.* **6**, 28450 (2016)
 31. Duru, P., Hallez, Y.: A three-step scenario involved in particle capture on a pore edge. *Langmuir* **31**(30), 8310 (2015)
 32. Zimmermann, U., Smallenburg, F., Löwen, H.: Flow of colloidal solids and fluids through constrictions: dynamical density functional theory versus simulation. *J. Phys. Condens. Matter* **28**, 244019 (2016)
 33. Sendekie, Z.B., Bacchin, P.: Colloidal Jamming dynamics in microchannel bottlenecks. *Langmuir* **32**(6), 1478 (2016)
 34. Mann, H., Mueller, P., Hagemeyer, T., Roloff, C., Thévenin, D.: Analytical description of the unsteady settling of spherical particles in Stokes and Newton regimes. *J. Tomas Granul. Matter* **17**, 629 (2015)
 35. Ganatos, P., Pfeffer, R., Weinbaum, S.: A strong interaction theory for the creeping motion of a sphere between plane parallel boundaries. Part 2. Parallel motion. *J. Fluid Mech.* **99**, 755 (1980)
 36. Arsenijević, Z., Grbavčić, Z., Garić-Grulović, R., Bošković-Vragolović, N.: Wall effects on the velocities of a single sphere settling in a stagnant and counter-current fluid and rising in a co-current fluid. *Powder Technol.* (2010)
 37. Zenit, R., Hunt, M.L.: Mechanics of immersed particle collisions. *J. Fluids Eng.* **121**, 179 (1999)
 38. Gondret, P., Lance, M., Petit, L.: Experiments on the motion of a solid sphere toward a wall: from viscous dissipation to elastohydrodynamic bouncing. *Phys. Fluids* **11**, 2803 (1999)
 39. Izar, E., Bonometti, T., Lacaze, L.: Modelling the dynamics of a sphere approaching and bouncing on a wall in a viscous fluid. *J. Fluid Mech.* **747**, 422 (2014)
 40. Kim, S., Karrila, S.: *Microhydrodynamics: principles and selected applications*. Dover Publications, Mineola (2005)
 41. Ganatos, P., Pfeffer, R., Weinbaum, S.: A strong interaction theory for the creeping motion of a sphere between plane parallel boundaries. Part 1. Perpendicular motion. *J. Fluid Mech.* **99**, 739–753 (1980)
 42. Kloss, C., Goniva, C., Hager, A., Amberger, S., Pirker, S.: A strong interaction theory for the creeping motion of a sphere between plane parallel boundaries. Part I. Perpendicular motion. *Prog. Comput. Fluid Dyn.* **12**, 140 (2012)
 43. Weller, H., Tabor, G., Jasak, H., Fureby, C.: A tensorial approach to computational continuum mechanics using object-oriented techniques. *Comput. Phys.* **12**, 620 (1998)
 44. Fonceca, I., Maza, D., Hidalgo, R.C.: Modeling particle-fluid interaction in a coupled CFD-DEM framework. *EPJ Web Conf.* **249**, 09004 (2021)
 45. Municchi, F., Radl, S.: Consistent closures for Euler-Lagrange models of bi-disperse gas-particle suspensions derived from particle-resolved direct numerical simulations. *Int. J. Heat Mass Transf.* **111**, 2589 (2017)
 46. Gago, P.A., Raeini, A.Q., King, P.: A spatially resolved fluid-solid interaction model for dense granular packs/soft-sand. *Adv. Water Resour.* **136**, 103454 (2020)
 47. Goniva, C., Blais, B., Radl, S., Kloss, C.: Open source CFD-DEM modelling for particle-based processes. In: *Eleventh International Conference on CFD in the Minerals and Process Industries* (2015)
 48. Dressaire, E., Sauret, A.: Clogging of microfluidic systems. *Soft Matter* **13**, 8597 (2017)

Publisher's Note Springer Nature remains neutral with regard to jurisdictional claims in published maps and institutional affiliations.